electrochem

MDPI

Article

Nanowire Electrode Structures Enhanced Direct Extracellular Electron Transport via Cell-Surface Multi-Heme Cytochromes in *Desulfovibrio ferrophilus* IS5

Xiao Deng [1,*], Wipakorn Jevasuwan [2], Naoki Fukata [2] and Akihiro Okamoto [1,3,4,5,*]

[1] Research Center for Macromolecules and Biomaterials, National Institute for Materials Science, 1-1 Namiki, Tsukuba 305-0044, Japan
[2] Research Center for Materials Nanoarchitectonics, National Institute for Materials Science, 1-1 Namiki, Tsukuba 305-0044, Japan; jevasuwan.wipakorn@nims.go.jp (W.J.); fukata.naoki@nims.go.jp (N.F.)
[3] Graduate School of Chemical Sciences and Engineering, Hokkaido University, North 13 West 8, Kita-ku, Sapporo 060-8628, Japan
[4] Graduate School of Science and Engineering, College of Science and Engineering, University of Tsukuba, 1-1-1 Tennodai, Tsukuba 305-8573, Japan
[5] Living Systems Materialogy (LiSM) Research Group, International Research Frontiers Initiative (IRFI), Tokyo Institute of Technology, 4259 Nagatsuta, Midori-ku, Yokohama 226-8503, Japan
* Correspondence: deng.xiao@nims.go.jp (X.D.); okamoto.akihiro@nims.go.jp (A.O.)

Abstract: Extracellular electron transfer (EET) by sulfate-reducing bacteria (SRB), such as *Desulfovibrio ferrophilus* IS5, enables bacterial interactions with minerals, which are vital for biogeochemical cycling and environmental chemistry. Here, we explore the direct EET mechanisms through outer-membrane cytochromes (OMCs) using IS5 as a model SRB. We employed nanostructured electrodes arrayed with 0, 50, 200, and 500 nm long nanowires (NWs) coated with indium–tin–doped oxide to examine the impact of electrode morphology on the direct EET efficacy. Compared to flat electrodes, NW electrodes significantly enhanced current production in IS5 with OMCs. However, this enhancement was diminished when OMC expression was reduced. Differential pulse voltammetry revealed that NW electrodes specifically augmented redox peaks associated with OMCs without affecting those related to redox mediators, suggesting that NWs foster direct EET through OMCs. Scanning electron microscopy observations following electrochemical analyses revealed a novel vertical cell attachment and aggregation on NW electrodes, contrasting with the horizontal monolayer cell attachment on flat electrodes. This study presents the first evidence of the critical role of electrode nanoscale topography in modulating SRB cell orientation and aggregation behavior. The findings underscore the significant influence of electrode morphology on the direct EET kinetics, highlighting the potential impact of mineral morphology on mineral reduction and biogeochemical processes.

Keywords: cell attachment; differential pulse voltammetry; electrochemical analysis; nanostructure; outer-membrane cytochrome; scanning electron microscopy

Citation: Deng, X.; Jevasuwan, W.; Fukata, N.; Okamoto, A. Nanowire Electrode Structures Enhanced Direct Extracellular Electron Transport via Cell-Surface Multi-Heme Cytochromes in *Desulfovibrio ferrophilus* IS5. *Electrochem* **2024**, *5*, 330–340. https://doi.org/10.3390/electrochem5030021

Academic Editor: Masato Sone

Received: 1 July 2024
Revised: 31 July 2024
Accepted: 7 August 2024
Published: 13 August 2024

1. Introduction

Extracellular electron transfer (EET) is a process by which microbes transport intracellular electrons, derived from metabolic reactions, to external solid electron acceptors such as metal oxides, anodes, or other microbial cells [1]. This respiratory mechanism, which significantly expands microbial metabolic flexibility, is critical for microbes encountering conditions with limited soluble electron acceptors and contributes to global biogeochemical cycles [2,3]. Furthermore, EET has been pivotal in developing various biotechnological applications, including microbial fuel cells (MFCs) for organic wastewater treatment and power generation [1,4,5]. Given its importance, EET mechanisms have been extensively studied, particularly in iron-reducing bacteria such as *Shewanella* and *Geobacter* species [1]. In contrast, despite sulfate-reducing bacteria (SRB) playing a major role in regulating

Fe(III) reduction and environmental chemistry in many anaerobic settings [6,7], their EET capabilities and mechanisms have only begun to be appreciated in recent years [8]. In particular, *Desulfovibrio ferrophilus* IS5, a SRB strain possessing outer-membrane cytochromes (OMCs) with multi heme redox centers, has served as the model bacterium [9,10]. The electrochemical analysis of strain IS5 on positively poised electrode as the sole electron acceptor has suggested that IS5 can transport electrons derived from lactate-oxidation to electrodes via OMCs [9]. Additionally, it may secrete unknown redox mediators to shuttle indirect electron transfer with the electrode [9]. These proposed mechanisms align with observations of Fe(III) oxide reduction by IS5 at slower rates when the oxides are occluded in porous alginate beads, permitting the diffusion of redox mediators but limiting direct cell access to the mineral [10].

While SRB use solid electron acceptors with various surface morphologies, the impact of these morphologies on SRB EET performance is still unknown. However, modifying electrode surface morphology has been widely applied to regulate the EET rates of other bacterial species, particularly to enhance MFC performance [11,12]. Nanostructures on electrodes, such as nanoporous conductive polymer [poly(3,4-ethylenedioxythiophene), PEDOT], Sn-doped In_2O_3 nanowire arrays, and polypyrrole nanowire arrays, significantly improved EEU in *Shewanella* by enhancing cell attachment to the electrode and altering the redox state and OMCs and interfacial electron transfer kinetics [13–15]. Additionally, when an external gravitational force was applied, nanorods were shown to penetrate the *Shewanella* membrane and function as a new OMCs-independent EET pathway [16]. Moreover, these high-aspect-ratio nanostructures typically possess high sensitivity towards surface-adsorbed species [17], but not the diffusing electron mediators, underlining the critical role of OMCs in mediating EET in *Shewanella* [18].

Here, we study the impact of electrode surface morphology on the kinetic and mechanism of EET in IS5, employing Si nanowires (NWs) of lengths varying from 0 to 500 nm, sputter coated by a 20 nm thick layer of indium–tin–doped oxide (ITO). We used this NW-arrayed electrodes to investigate how the nanostructure impacts the direct EET process via OMCs of *D. ferrophilus* IS5. Microbial interaction with electrode was studied by voltammetry analyses and scanning electron microscopy (SEM). Our study provides the first insight into the relationship between solid surface morphology and the EET mechanism in SRB, which has critical implications for the dynamics of biogeochemical cycling and environmental chemistry.

2. Material and Methods

2.1. Fabrication of NW Arrayed Electrodes

NW arrays were fabricated on boron-doped *p*-Si(100) substrates with a resistivity of 0.0065–0.0084 Ω·cm and wafer thickness of 725 μm via metal catalyst electroless etching [19,20]. In detail, the Si substrates were first cut into 3 cm × 3 cm sizes. Subsequently, they underwent ultrasonic cleaning in acetone, isopropyl alcohol, and deionized (DI) water, each for 10 min. Then, the samples were immersed in piranha solution [H_2O_2 (30%):H_2SO_4 (96%) = 3:1 (v/v)] for 20 min at 120 °C and rinsed with DI water until pH = 5. The surface oxide was removed by etching with a 1% HF solution for 2 min and immediately dipped into a 0.02 M $AgNO_3$ solution in 4.8 M HF for various etching times of 30 s, 1 min 30 s, and 3 min to form NW lengths of 50 nm, 200 nm, and 500 nm, respectively. Ag dendrites, formed during the chemical reaction, were removed from NWs by dipping the samples in 30% HNO_3 for 5 min and then rinsing them with DI water. Finally, to remove any remaining surface oxide, the samples were further etched in 1% HF for 2 min. After that, a 20 nm-thick ITO film was deposited onto the NW structures by sputtering at a radio frequency power of 100 W using a CFS-4EP sputter (SHIBAURA, Kanagawa, Japan). To fabricate the flat electrode, which served as the negative control without NW arrays, a 20 nm thick ITO film was sputter-coated onto the same boron-doped *p*-Si(100) substrate as described above.

2.2. Cultivation of Strain IS5

Desulfovibrio ferrophilus IS5 was routinely cultivated at 28 °C for 5 days in a 100 mL glass vial containing 80 mL of the DSMZ medium 195c, under a headspace of N_2 and CO_2 (80:20), with an inoculum ratio of 5% (v/v). The electron donor and acceptor contained in the DSMZ medium 195c were 22.3 mM Na-L-lactate and 21 mM sulfate, respectively. As previously reported, strain IS5 has a doubling time of approximately 13.5 h and enters the stationary phase after two days of cultivation in this medium [21]. After 5 days of cultivation under this condition, IS5 cells were lactate-starved and highly expressed OMCs on their surface [21]. To obtain IS5 cells with low OMC expression, IS5 was grown for 5 days in a modified medium 195c containing an excess of Na-L-lactate (111.5 mM) as the electron donor, a condition that significantly down-regulates OMC expression [21].

2.3. SEM

A SU8000 microscope (Hitachi, Tokyo, Japan) was used to observe the NW arrays with ITO coating after fabrication, and IS5 cells attached to the electrodes following electrochemical analyses. To observe the NW arrays, the electrode was attached to the SEM sample holder using carbon tape and then subjected to observation. For observing IS5 on electrodes after electrochemical analyses, the electrodes were carefully removed from the reactors and immediately fixed by immersion in 2.5% (v/v) glutaraldehyde prepared in phosphate buffer (PB, 100 mM, pH = 7) for 1 h. After fixation, the electrodes were washed three times by immersion in PB for 8 min per wash. The samples were then dehydrated in ethanol gradients (25%, 50%, and 75% v/v) prepared in ultrapure water and pure ethanol for 8 min per concentration. Subsequently, the pure ethanol was exchanged three times with *t*-butanol, frozen in a −20 °C freezer for 15 min, and then freeze-dried under vacuum. Finally, evaporated platinum was coated on the dried samples using a Quick Coater SC-701 (Sanyu Denshi KK, Nishi-ku, Nagoya, Japan) before being attached to the SEM sample holder using carbon tape and being viewed under a SU8000 microscope.

2.4. Water Contact Angle Measurement

The water contact angles of the flat and NW electrodes were measured with a VCA Optima-XE instrument (AST Products Inc., Billerica, MA, USA). A microsyringe was used to place 2 µL of ultrapure water onto the electrode surface for the measurement. Three points across each electrode surface were measured.

2.5. Electrochemical Analysis

All electrochemical analyses were conducted at 28 °C in single-chamber, three-electrode reactors inside a COY anaerobic chamber filled with 100% N_2, using a potentiostat (VMP3, Bio Logic Company, Seyssinet-Pariset, France). The fabricated flat and NW arrayed electrodes were placed at the bottom and served as the working electrode. An Ag/AgCl (saturated KCl) electrode and a platinum wire were used as the reference and counter electrode, respectively.

For the cyclic voltammetry of potassium ferric cyanide, we prepared a 1 mM solution in 1 M KCl, sterilized it by filtration through 0.22 µm pore-size filters, and purged it with N_2 for 30 min. Then, 5 mL of this solution was added to each reactor for cyclic voltammetry analysis at a scan rate of 10 mV/s.

For measuring EET process of IS5, the electrolyte composition included 457 mM NaCl, 47 mM $MgCl_2 \cdot 6H_2O$, 7 mM KCl, 30 mM $NaHCO_3$, 1 mM $CaCl_2 \cdot 2H_2O$, 1 mM K_2HPO_4, 1 mM NH_4Cl, 25 mM Na^+-HEPES (pH 7.4), 1 mL selenite–tungstate solution (12.5 mM NaOH, 11.4 mM Na_2SeO_3, and 12.1 mM $Na_2WO_4 \cdot 2H_2O$), and 1 mL trace element SL-10 solution. Additionally, 22.3 mM Na-L-lactate was added as the electron donor. The electrolyte was rigorously purged with N_2 for 30 min, autoclaved, and then purged again with N_2 for an additional 15 min before use. Lactate-starved and lactate-sufficient IS5 cells were harvested from the 5-day-old liquid culture by centrifugation (7800× g for 10 min) inside the anaerobic chamber. The cell pellets were resuspended in the anoxic electrolyte and then

added to reactors containing 4.9 mL of electrolyte, achieving a final OD_{600nm} of 0.5 and a final volume of 5 mL. Single-potential amperometry was performed with the electrodes being poised at +0.4 V vs. SHE. Differential pulse (DP) voltammetry was conducted with 5.0 mV pulse increment, 50 mV pulse amplitude, 300 ms pulse width, and 5.0 s pulse period. The potential was scanned towards the positive direction. The background of DP voltammograms was subtracted using the software QSoas version 3.1 [22].

3. Results

NWs with lengths varying from 50 nm, 200 nm, and 500 nm were fabricated on the Si surface following a previous report [19], and were then sputter-coated with a layer of 20 nm thick ITO to ensure good electrical conductivity (Figure 1A–D). In addition, we prepared the electrode without NWs, sputter-coating ITO on a flat Si surface, is referred to as the ITO electrode. SEM observation of the electrode surface revealed densely distributed NWs arrays. While some remined individual with diameters less than 30 nm, other NWs conjugated into nanowalls with narrow widths of less than 50 nm, similar to the observations made in the previous report [19]. These NW arrays were spaced several tens of nanometers apart, with the density decreasing slightly as NW lengths increased due to more Si being removed during the longer etching period. We found that the NW arrays improved the electrode's hydrophilicity as water contact angle decreased (Figure 1E), a trend that aligns with previous observations [23] and may promote cell attachment and EET in some bacteria [24,25].

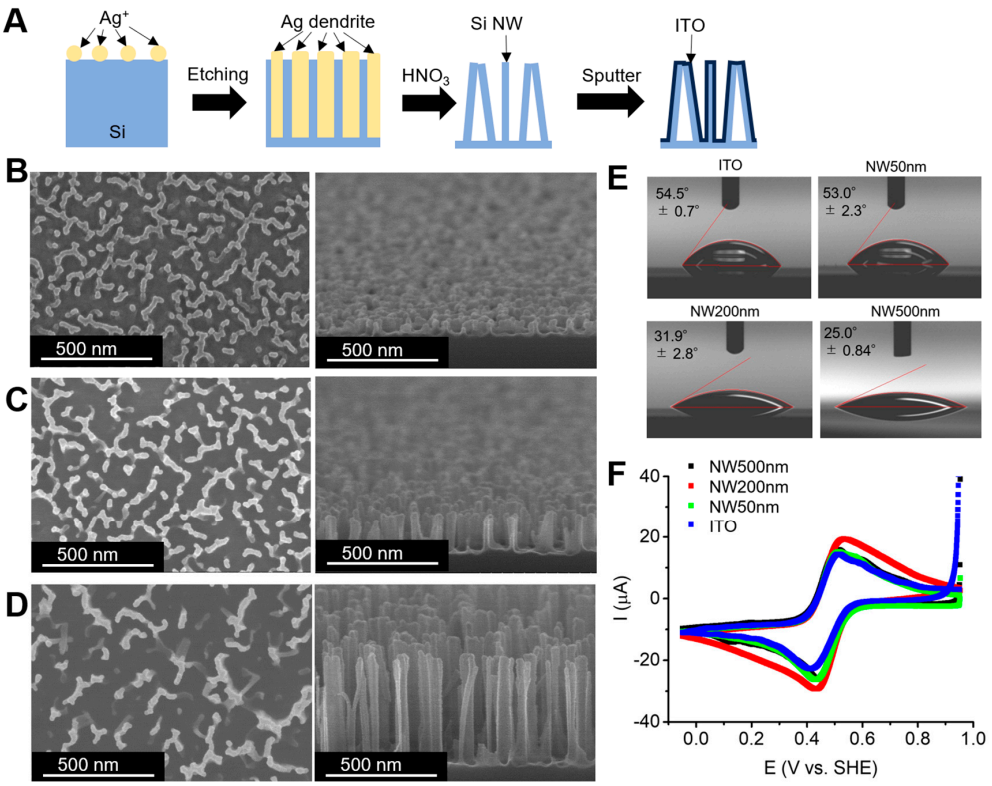

Figure 1. Preparation and characterization of NW arrayed electrodes. (**A**) Schematic illustration of the electrode fabrication process. (**B**–**D**) Top view and 45°-angle view SEM images of the ITO-coated NW arrays with lengths of 50 nm (**B**), 200 nm (**C**), and 500 nm (**D**). Due to the random etching by Ag^+ ions, NW arrays are heterogeneously formed on the surface, with some conjugating together. (**E**) Water contact angles of the NW arrayed electrode. NW50nm, NW200nm, and NW500nm refer to NW arrayed electrodes with lengths of 50 nm, 200 nm, and 500 nm, respectively. (**F**) Cyclic voltammograms of 1 mM sterile potassium ferricyanide prepared in 1 M KCl on NW electrodes. Scan rate = 10 mV s^{-1}.

The NW arrays did not appear to enhance redox reactions by soluble electron shuttles. Cyclic voltammetry of a standard 1 mM sterile ferric cyanide solution on the ITO and NW arrayed electrodes demonstrated comparable redox peak heights (Figure 1F). The inability to increase mediator-shuttled redox reactions by nanostructures has also been reported with the porous PEDOT polymer [13]. This phenomenon may arise from the unique NW morphology combined with the absence of electrolyte stirring, causing diffusion limitations in the bottom parts of the NW arrays. As a result, only the top parts of the NWs act as the actual active surface area, which does not differ much from that of the flat electrode.

Next, we investigated how NW arrays influence the EET performance of strain IS5 by measuring its anodic current production. The ITO and NW arrayed electrodes were poised at +0.4 V to serve as the sole electron acceptor, with 22.3 mM of lactate as the sole electron donor. Strain IS5 was precultivated in its growth medium (DSMZ medium 195c) for 5 days, leading to lactate-starvation and OMC-overexpression conditions in the cells [21]. While the sterile electrolyte produced background currents of less than 5 nA cm^{-2} on all electrodes (Figure 2A), the introduction of OMCs-expressing IS5 onto the flat ITO electrode caused the anodic current to increase to approximately 90 nA cm^{-2} at 90 min, which then slightly decreased to 60 nA cm^{-2}, confirming the EET capability of IS5 [9]. In comparison, the NW arrayed electrodes exhibited an initial spike in current, followed by a sharp and continuous increase in current production, reaching significantly higher levels than on the flat ITO electrode. Specifically, the current produced 15 min after cell addition (approximately 0.2 μA cm^{-2}) was eight times higher on NW-arrayed electrodes. A similar number of IS5 cell attached to both the flat and NW-arrayed electrodes 15 min after cell addition (Figure 2B). Given NW arrays did not promote soluble mediator shuttled redox reactions (Figure 1F), the significant current enhancement by NW arrays following cell addition suggests that NW arrays significantly enhanced direct EET via OMCs.

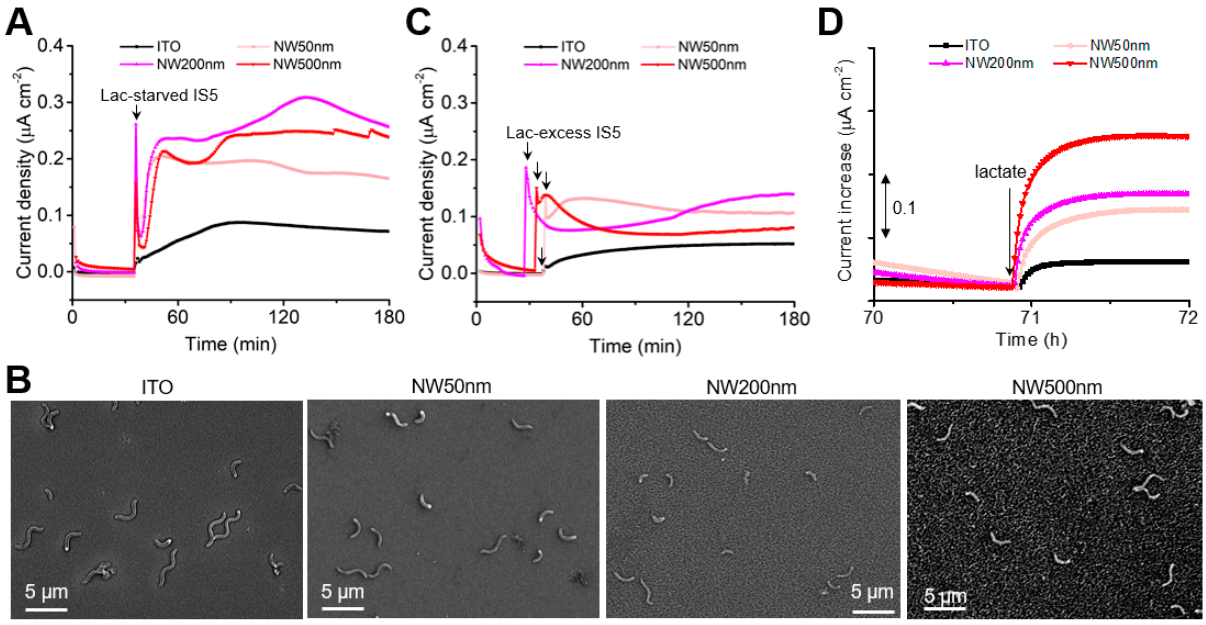

Figure 2. Electrochemical activity of lactate-starved and lactate-excess *D. ferrophilus* IS5 cells on NWs arrayed electrodes. (**A**) Current production by strain IS5 cells precultivated under a lactate-starved condition, which induces the OMC overexpression. (**B**) SEM images of the electrode surfaces 15 min after introducing lactate-starved cells into the reactors. (**C**) Current production by IS5 cells precultivated under a lactate-excess condition, which suppresses the OMC expression. (**D**) The effect of re-adding 22.3 mM lactate to the current production by IS5 cells, which were precultivated with insufficient lactate, approximately 71 h after the start of current measurement.

To test this hypothesis, we examined the EET enhancement effect on IS5 with low OMC expression levels. The current production by low-OMC-expressing IS5, obtained by precultivating with excess lactate [21], is shown in Figure 2C. The low-OMC-expressing IS5 did not cause a sharp increase in current after the initial spike, supporting our hypothesis that the steep current increase observed in lactate-starved IS5 was due to an accelerated direct EET process via strengthened electrochemical interactions between OMCs and NW arrays. Additionally, these cells displayed a slower and lower current rise on the flat ITO electrode compared to the OMCs-expressing IS5, indicating that OMCs are involved in the current production on the ITO electrode.

We additionally confirmed that lactate oxidation metabolism sources the anodic current on both flat and NW-arrayed electrodes. This was demonstrated by observing a positive current response upon the re-addition of lactate as the electron donor at 70.9 h, while current production by IS5 cells precultivated with insufficient lactate was decreasing due to lactate depletion (Figure 2D). Reintroducing lactate prompted the currents to increase by 0.04 to 0.24 μA cm^{-2} on flat and NW-arrayed electrodes.

To obtain direct evidence for strengthened electrochemical interactions between OMCs and NW arrays, we conducted the DP voltammetry of OMC-expressing IS5 at 180 min of current measurement (Figure 2A). At this point, the currents had maximized and stabilized, indicating that the OMCs had established a stable electrochemical interaction with the NW arrays. While the DP voltammograms of the sterile electrolyte lacked distinct peaks except for minor fluctuations in background currents on both the flat and NW electrodes (Figure 3A), the DP voltammogram of IS5 cells on the flat ITO revealed two broad peaks in the region of 0.2 to -0.1 V (peaked at 0.05 V) and -0.1 to -0.3 V (peaked at -0.22 V), respectively (Figure 3B). This voltammogram was almost identical to that in a previous study [9], which assigned each peak to self-secreted electron mediators and OMCs, respectively, based on their increased intensities over time and sensitivity to a heme-binding chemical, nitric oxide. In contrast, the DP voltammograms of IS5 on NW arrayed electrodes demonstrated a distinct "U"-shaped background, typically observed with high aspect ratio vertical nanostructured electrodes [26–28]. After subtracting the baseline, further details in the OMC peak and the significant amplification of this redox signal by NW arrays were clearly demonstrated (Figure 3C). In comparison to the small OMC peak on the flat ITO electrode, which showed a slight peak separation (Figure 3C inset), likely reflecting the multiple redox centers of the OMC complex [21], both the peak intensity and the peak separation were significantly amplified on NW electrodes. As the cell number on electrodes at the time of DP voltammetry remained comparable for all electrodes (Figure 3D), the enhanced OMCs redox signals on NW arrays indicate strengthened electrochemical interactions between OMCs and the electrodes. Baseline-subtracted DP voltammograms further revealed that the peak intensities of redox mediators remained almost unchanged across all electrodes, indicating that NW arrays did not enhance the mediated electron transfer process, consistent with the conclusion obtained by cyclic voltammetry of the ferric cyanide solution (Figure 1F).

Finally, to further understand the interfacial interaction between IS5 cells and NW arrays, we conducted SEM observations of cells on the electrodes from tilt-angle and side views. Tilt-angle and side-view observations revealed significant differences in the mode of cell attachment. While all observed IS5 cells, which are S-shaped bacteria, were horizontally attached to the flat electrode with a twist (Figure 4A), nearly half of the observed cells were vertically attached to or "arched" on the NW arrays (Figure 4B–D), indicating that cells sensed the electrode morphology and adjusted their attachment mechanism. The vertical attachment largely reduces the cell contact area with the electrode, which may reduce cell damage by NW penetration, as cell deaths have been reported with cells horizontally attached to NW-shaped materials [29]. Indeed, some horizontally attached IS5 cells appeared punctured by NW arrays, leaving only thin membranes on the NW arrays, compared to the intact cell morphology of vertically attached cells (Figure 4F). Furthermore, we observed multiple cells stacking atop the vertically attached cells, forming

cell aggregates on NW arrays (Figure 4E). Intercellular appendages were observed within these aggregates, resembling the bacteria nanowires produced by electroactive *Shewanella* and electron-extracting IS5, which contain abundant OMCs and are proposed to facilitate long-range EET [21,30,31]. Collectively, these observations suggest that IS5 favors the formation of electrically conductive cell aggregates on nanostructured solid surfaces to achieve a high EET rate.

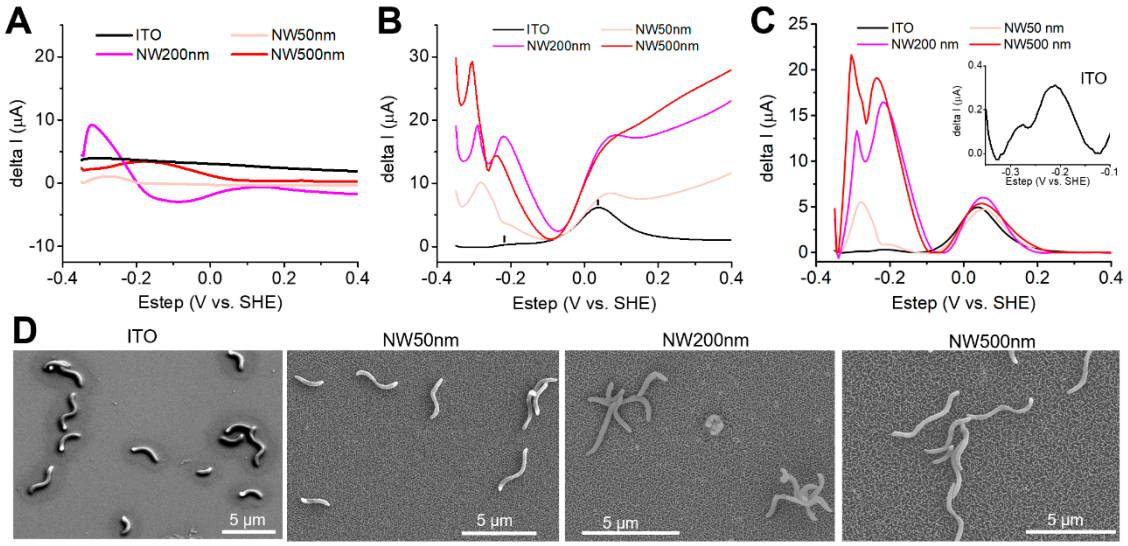

Figure 3. DP voltammetry and SEM observation of lactate-starved IS5 cells on NW-arrayed electrodes after 180 min of current measurement (as shown in Figure 2A). (**A**,**B**) DP voltammograms of sterile electrolytes (**A**) and IS5 cells (**B**). In panel (**B**), black short bars at −0.22 V and 0.05 V denote peaks associated with OMCs and cell-secreted redox mediators, respectively. (**C**) Baseline-subtracted DP voltammograms of IS5 cells. Inset panel depicts the enlarged voltammogram of IS5 on flat ITO electrode, focusing on the region (−0.1 to −0.35 V) associated with OMCs. (**D**) SEM images of cells attached on the electrode surface after the electrochemical analysis.

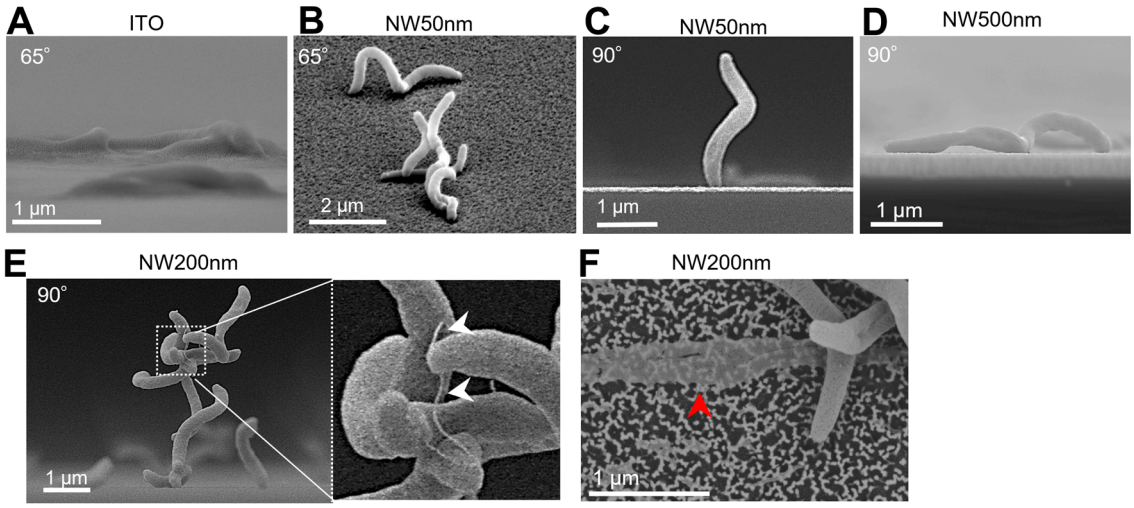

Figure 4. (**A**–**E**) Tilt-angle and side-view SEM images of IS5 cells on flat and NW-arrayed electrodes after 180 min of current measurement (as shown in Figure 2A). Top view SEM images of the same samples are shown in Figure 3D. In panel (**E**), white arrows indicate appendages extending from IS5 cells and bridging with other cells. (**F**) a horizontally attached, ruptured cell observed on the NW200nm electrode, as indicated by the red arrow.

4. Discussion

While flat electrode surface materials have facilitated the analysis of the EET mechanisms in SRB, the insoluble substances available in natural environments, which may be reduced by SRB or conduct electrons to them, possess complex nanostructures [32–35], contrasting starkly to the flat electrodes. However, how nanostructures impact the EET performance of SRB remains unknown. The EET kinetics of IS5 depend on multiple factors, including lactate availability, OMCs expression levels, cell aggregate formation, and the secretion of redox mediators. Nonetheless, by focusing on the EET performance shortly after cell addition, we were able to evaluate the effect of electrode nanostructures while keeping these factors consistent across all reactors. Our results revealed that electrode nanostructures significantly enhanced the direct EET process via OMCs immediately after cell addition, even though the cell contact area with electrodes seemed to decrease as many cells attached vertically to the NW arrays. Although the cell number and the number of OMCs per cell remain the same for the flat and NW arrayed electrodes, NW arrays detected higher redox signals associated with OMCs, indicating significantly stronger electrochemical interactions between OMCs and the electrode, which is key for EET acceleration. We propose that such strengthened interaction is due to the closer positioning of OMCs to the NW arrays, whereas the OMCs of the S-shaped IS5 cells only interact strongly at limited positions on flat electrodes (Figure 5). These results also suggest that SRB may reduce nanowire-structured minerals more rapidly than those with a smooth surface in natural environments.

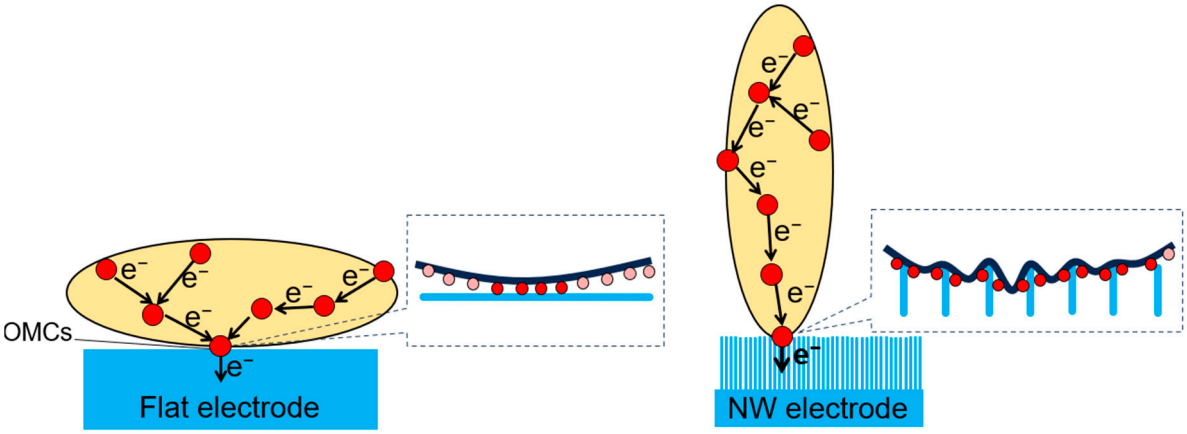

Figure 5. Schematic illustration of enhanced electrochemical interactions between OMCs and NW arrays. While IS5 horizontally attaches to the flat electrode, the curved cell shape causes weak contact of OMCs with the flat electrode surface. In comparison, when IS5 vertically attaches to the NW arrays, the position of NWs against the outer membrane causes close contact of OMCs with the electrode, leading to much stronger electrochemical interactions. Red and pink circles indicate OMCs in strong and weak electrochemical interactions with the electrodes, respectively. Although the total number of OMCs possessed by a cell on the flat or NW arrayed electrode is the same, the stronger interaction of the OMCs with NW arrays results in higher redox signals detected on the NW arrayed electrode.

Our measured redox potential of IS5 OMCs under anodic EET condition (approximately −0.2 V) was consistent with a previous study [9] and was more than 200 mV more positive than that measured for OMCs under cathodic electron-uptake conditions [21,25]. This difference aligns with observations in *S. oneidensis* OMCs under anodic and cathodic conditions, caused by the redox bifurcation of the flavin-binding cofactor in the OMCs [36]. Therefore, the IS5 OMCs may contain an electron-bifurcating cofactor. Alternatively, this result suggests that IS5 employs different OMCs for each process.

SEM observations revealed that NW arrays facilitated vertical cell attachment, which promoted cell aggregation. Vertical attachment and stacking at polar and curved cell positions suggest the presence of adhesive proteins, such as adhesins, at these positions,

providing an explanation for why polar-positioned cells facilitate cell aggregation more than horizontally attached cells. However, further studies are needed to identify the specific mechanisms regulating cell attachment styles on different surfaces. For example, a comparative analysis of genes involved in biofilm formation on flat and NW electrodes could provide molecular-level insights. Moreover, the future testing of cell attachment on NWs arrays with other bacterial strains besides IS5 would help clarify the generality of our findings and facilitate comparative mechanistic studies. SEM also showed that some horizontally attached cells ruptured on NW arrays, suggesting that some cells were penetrated and damaged by sharp NWs, similar to previous findings with nanorod and nanopillar materials [37–39]. While the small diameters of the individual NWs are comparable to membrane-penetrable structures [40,41], confirming membrane penetration requires the further cross-sectional observations of the cell-NW interface and modelling analysis [29,42]. Additionally, our observations of cell appendages within aggregates but not in monolayer-attached cells suggest that these appendages may impact biofilm formation and long-range electron transfer [21,30,31]. Further investigation is needed through electric conductivity measurements [43,44] and OMCs distribution observations [21,45,46]. These findings offer new insights into biofilm formation mechanisms and material development to inhibit the formation of biofilms, which deteriorate metals and exhibit resistance to biocides and antibiotics [47–49].

5. Conclusions

Our results demonstrate that NW arrays significantly enhanced the direct EET process via OMCs in strain IS5 but not the cell attachment or redox mediator shuttled process. An eight- to ten-fold enhancement in current production was observed on NW arrays compared to flat ITO electrodes within 15 min of cell addition. This enhancement was weakened in IS5 with low OMC-expression levels, underscoring the importance of OMCs in the EET process. SEM observations revealed reduced direct cell contact area with NW arrays due to vertical attachment. Yet, much higher redox signals associated with OMCs were recorded, indicating that the electrochemical and molecular-level interactions between OMCs and NW arrays were significantly promoted, leading to EET acceleration even with fewer OMCs directly adsorbed on the electrode surface. These results provide new insights into the reduction kinetics of natural minerals with nanostructured surfaces and the SRB biofilm formation mechanism. Given their ability to specifically amplify the redox signals of surface adsorbed species, NW arrays may be used to analyze redox signals in bacterial strains with low-current production capabilities or low cell densities.

Author Contributions: X.D.: conceptualization, methodology, validation, formal analysis, investigation, data curation, writing—original draft preparation, writing—review and editing, funding acquisition. W.J.: methodology, data curation, writing—review and editing. N.F.: methodology, writing—review and editing. A.O.: methodology, writing—review and editing. All authors have read and agreed to the published version of the manuscript.

Funding: This research was funded by the Murata Science and Education Foundation, Kyoto, Japan (for X.D.), JSPS KAKENHI (22H02265, 22KK0242, 23K23532 for A.O.), and JAEA Nuclear Energy S&T and Human Resource Development Project through concentrating wisdom [grant number JPJA20P20333393].

Institutional Review Board Statement: Not applicable.

Informed Consent Statement: Not applicable.

Data Availability Statement: The original contributions presented in the study are included in the article; further inquiries can be directed to the corresponding authors.

Acknowledgments: The authors are thankful for the use of sputtering instrument and SEM at the NIMS nanofabrication facility and for the contact angle measurement instrument at the NIMS Molecule & Material Synthesis Platform, which is operated by the Ministry of Education, Culture, Sports, Science and Technology (MEXT), Japan (No. JPMXP09SyyNMnnnn).

Conflicts of Interest: The authors declare no conflicts of interest.

References

1. Shi, L.; Dong, H.; Reguera, G.; Beyenal, H.; Lu, A.; Liu, J.; Yu, H.-Q.; Fredrickson, J.K. Extracellular electron transfer mechanisms between microorganisms and minerals. *Nat. Rev. Microbiol.* **2016**, *14*, 651–662. [CrossRef] [PubMed]
2. Myers, C.R.; Nealson, K.H. Bacterial manganese reduction and growth with manganese oxide as the sole electron-acceptor. *Science* **1988**, *240*, 1319–1321. [CrossRef]
3. Lovley, D.R.; Phillips, E.J.P. Novel Mode of Microbial Energy Metabolism: Organic Carbon Oxidation Coupled to Dissimilatory Reduction of Iron or Manganese. *Appl. Environ. Microbiol.* **1988**, *54*, 1472–1480. [CrossRef] [PubMed]
4. Logan, B.E.; Rossi, R.; Ragab, A.; Saikaly, P.E. Electroactive microorganisms in bioelectrochemical systems. *Nat. Rev. Microbiol.* **2019**, *17*, 307–319. [CrossRef] [PubMed]
5. Lovley, D.R. Bug juice: Harvesting electricity with microorganisms. *Nat. Rev. Microbiol.* **2006**, *4*, 497–508. [CrossRef] [PubMed]
6. Coleman, M.L.; Hedrick, D.B.; Lovley, D.R.; White, D.C.; Pye, K. Reduction of Fe(III) in sediments by sulphate-reducing bacteria. *Nature* **1993**, *361*, 436–438. [CrossRef]
7. Barton, L.L.; Fauque, G.D. Biochemistry, physiology and biotechnology of sulfate-reducing bacteria. *Adv. Appl. Microbiol.* **2009**, *68*, 41–98. [CrossRef] [PubMed]
8. Murugan, M.; Miran, W.; Masuda, T.; Lee, D.S.; Okamoto, A. Biosynthesized Iron Sulfide Nanocluster Enhanced Anodic Current Generation by Sulfate Reducing Bacteria in Microbial Fuel Cells. *ChemElectroChem* **2018**, *5*, 4015–4020. [CrossRef]
9. Deng, X.; Okamoto, A. Direct extracellular electron transfer to an indium tin doped oxide electrode via heme redox reactions in *Desulfovibrio ferrophilus* IS5. *Electrochim. Acta* **2023**, *453*, 142293. [CrossRef]
10. Liang, D.; Liu, X.; Woodard, T.L.; Holmes, D.E.; Smith, J.A.; Nevin, K.P.; Feng, Y.; Lovley, D.R. Extracellular Electron Exchange Capabilities of *Desulfovibrio ferrophilus* and *Desulfopila corrodens*. *Environ. Sci. Technol.* **2021**, *55*, 16195–16203. [CrossRef]
11. Wang, R.; Li, H.; Sun, J.; Zhang, L.; Jiao, J.; Wang, Q.; Liu, S. Nanomaterials Facilitating Microbial Extracellular Electron Transfer at Interfaces. *Adv. Mater.* **2021**, *33*, 2004051. [CrossRef]
12. Li, Y.; Liu, J.; Chen, X.; Wu, J.; Li, N.; He, W.; Feng, Y. Tailoring Surface Properties of Electrodes for Synchronous Enhanced Extracellular Electron Transfer and Enriched Exoelectrogens in Microbial Fuel Cells. *ACS Appl. Mater. Interfaces* **2021**, *13*, 58508–58521. [CrossRef]
13. Liu, X.; Wu, W.; Gu, Z. Poly (3,4-ethylenedioxythiophene) promotes direct electron transfer at the interface between *Shewanella loihica* and the anode in a microbial fuel cell. *J. Power Sources* **2015**, *277*, 110–115. [CrossRef]
14. Bian, R.; Jiang, Y.; Wang, Y.; Sun, J.; Hu, J.; Jiang, L.; Liu, H. Highly Boosted Microbial Extracellular Electron Transfer by Semiconductor Nanowire Array with Suitable Energy Level. *Adv. Funct. Mater.* **2018**, *28*, 1707408. [CrossRef]
15. Ding, C.; Liu, H.; Lv, M.; Zhao, T.; Zhu, Y.; Jiang, L. Hybrid bio-organic interfaces with matchable nanoscale topography for durable high extracellular electron transfer activity. *Nanoscale* **2014**, *6*, 7866–7871. [CrossRef]
16. Rehnlund, D.; Lim, G.; Philipp, L.A.; Gescher, J. Nanowired electrodes as outer membrane cytochrome-independent electronic conduit in *Shewanella oneidensis*. *iScience* **2022**, *25*, 103853. [CrossRef]
17. Patolsky, F.; Zheng, G.; Lieber, C.M. Nanowire Sensors for Medicine and The Life Sciences. *Nanomedicine* **2006**, *1*, 51–65. [CrossRef]
18. Ding, C.-m.; Lv, M.-l.; Zhu, Y.; Jiang, L.; Liu, H. Wettability-Regulated Extracellular Electron Transfer from the Living Organism of *Shewanella loihica* PV-4. *Angew. Chem. Int. Ed.* **2015**, *54*, 1446–1451. [CrossRef]
19. Jevasuwan, W.; Nakajima, K.; Sugimoto, Y.; Fukata, N. Metal-catalyzed electroless etching and nanoimprinting silicon nanowire-based solar cells: Silicon nanowire defect reduction and efficiency enhancement by two-step H_2 annealing. *Jpn. J. Appl. Phys.* **2016**, *55*, 065001. [CrossRef]
20. Jevasuwan, W.; Pradel, K.C.; Subramani, T.; Chen, J.; Takei, T.; Nakajima, K.; Sugimoto, Y.; Fukata, N. Diffused back surface field formation in combination with two-step H_2 annealing for improvement of silicon nanowire-based solar cell efficiency. *Jpn. J. Appl. Phys.* **2017**, *56*, 04CP01. [CrossRef]
21. Deng, X.; Dohmae, N.; Nealson, K.H.; Hashimoto, K.; Okamoto, A. Multi-heme cytochromes provide a pathway for survival in energy-limited environments. *Sci. Adv.* **2018**, *4*, eaao5682. [CrossRef] [PubMed]
22. Fourmond, V. QSoas: A Versatile Software for Data Analysis. *Anal. Chem.* **2016**, *88*, 5050–5052. [CrossRef] [PubMed]
23. Sharma, V.; Yiannacou, K.; Karjalainen, M.; Lahtonen, K.; Valden, M.; Sariola, V. Large-scale efficient water harvesting using bioinspired micro-patterned copper oxide nanoneedle surfaces and guided droplet transport. *Nanoscale Adv.* **2019**, *1*, 4025–4040. [CrossRef] [PubMed]
24. Krasowska, A.; Sigler, K. How microorganisms use hydrophobicity and what does this mean for human needs? *Front. Cell. Infect. Microbiol.* **2014**, *4*, 112. [CrossRef] [PubMed]
25. Deng, X.; Luo, D.; Okamoto, A. Electrode hydrophilicity enhanced the rate of extracellular electron uptake in *Desulfovibrio ferrophilus* IS5. *Electrochim. Acta* **2022**, *421*, 140504. [CrossRef]
26. Remes, A.; Manea, F.; Motoc, S.; Baciu, A.; Szerb, E.I.; Gascon, J.; Gug, G. Highly Sensitive Non-Enzymatic Detection of Glucose at MWCNT-CuBTC Composite Electrode. *Appl. Sci.* **2020**, *10*, 8419. [CrossRef]
27. Dai, H.; Chen, D.; Li, Y.; Cao, P.; Wang, N.; Lin, M. Voltammetric sensing of dopamine based on a nanoneedle array consisting of $NiCo_2S_4$ hollow core-shells on a nickel foam. *Mikrochim. Acta* **2018**, *185*, 157. [CrossRef] [PubMed]

28. Uwimbabazi, E.; Mukasekuru, M.R.; Sun, X. Glucose Biosensor Based on a Glassy Carbon Electrode Modified with Multi-Walled Carbon Nanotubes-Chitosan for the Determination of Beef Freshness. *Food Anal. Methods* **2017**, *10*, 2667–2676. [CrossRef]
29. Jenkins, J.; Mantell, J.; Neal, C.; Gholinia, A.; Verkade, P.; Nobbs, A.H.; Su, B. Antibacterial effects of nanopillar surfaces are mediated by cell impedance, penetration and induction of oxidative stress. *Nat. Commun.* **2020**, *11*, 1626. [CrossRef]
30. Leung, K.M.; Wanger, G.; El-Naggar, M.Y.; Gorby, Y.; Southam, G.; Lau, W.M.; Yang, J. *Shewanella oneidensis* MR-1 Bacterial Nanowires Exhibit *p*-Type, Tunable Electronic Behavior. *Nano Lett.* **2013**, *13*, 2407–2411. [CrossRef]
31. Han, T.H.; Parveen, N.; Shim, J.H.; Nguyen, A.T.N.; Mahato, N.; Cho, M.H. Ternary Composite of Polyaniline Graphene and TiO_2 as a Bifunctional Catalyst to Enhance the Performance of Both the Bioanode and Cathode of a Microbial Fuel Cell. *Ind. Eng. Chem. Res.* **2018**, *57*, 6705–6713. [CrossRef]
32. Li, J.; Cui, J.; Yang, Q.; Cui, G.; Wei, B.; Wu, Z.; Wang, Y.; Zhou, H. Oxidative Weathering and Microbial Diversity of an Inactive Seafloor Hydrothermal Sulfide Chimney. *Front. Microbiol.* **2017**, *8*, 1378. [CrossRef] [PubMed]
33. Khan, Y.; Durrani, S.K.; Mehmood, M.; Khan, M.R. Mild hydrothermal synthesis of γ-MnO_2 nanostructures and their phase transformation to α-MnO_2 nanowires. *J. Mater. Res.* **2011**, *26*, 2268–2275. [CrossRef]
34. Zhu, H.; Deng, J.; Chen, J.; Yu, R.; Xing, X. Growth of hematite nanowire arrays during dense pentlandite oxidation. *J. Mater. Chem. A* **2014**, *2*, 3008–3014. [CrossRef]
35. Liu, M.; Zhang, G. Amorphous Goethite as a Catalyst of Chemoselectivity Epoxidation of Alkenes by Hydrogen Peroxide. *Russ. J. Gen. Chem.* **2022**, *92*, 1539–1545. [CrossRef]
36. Okamoto, A.; Hashimoto, K.; Nealson, K.H. Flavin redox bifurcation as a mechanism for controlling the direction of electron flow during extracellular electron transfer. *Angew. Chem. Int. Ed.* **2014**, *53*, 10988–10991. [CrossRef] [PubMed]
37. Cao, B.; Zhao, Z.; Peng, L.; Shiu, H.-Y.; Ding, M.; Song, F.; Guan, X.; Lee, C.K.; Huang, J.; Zhu, D.; et al. Silver nanoparticles boost charge-extraction efficiency in *Shewanella* microbial fuel cells. *Science* **2021**, *373*, 1336–1340. [CrossRef] [PubMed]
38. Seong, H.; Higgins, S.G.; Penders, J.; Armstrong, J.P.K.; Crowder, S.W.; Moore, A.C.; Sero, J.E.; Becce, M.; Stevens, M.M. Size-Tunable Nanoneedle Arrays for Influencing Stem Cell Morphology, Gene Expression, and Nuclear Membrane Curvature. *ACS Nano* **2020**, *14*, 5371–5381. [CrossRef]
39. Ivanova, E.P.; Hasan, J.; Webb, H.K.; Gervinskas, G.; Juodkazis, S.; Truong, V.K.; Wu, A.H.F.; Lamb, R.N.; Baulin, V.A.; Watson, G.S.; et al. Bactericidal activity of black silicon. *Nat. Commun.* **2013**, *4*, 2838. [CrossRef]
40. Nakamura, H.; Watano, S. Direct Permeation of Nanoparticles across Cell Membrane: A Review. *KONA Powder Part. J.* **2018**, *35*, 49–65. [CrossRef]
41. Zou, J.; Li, J.; Chen, T.; Li, X. Penetration mechanism of cells by vertical nanostructures. *Phys. Rev. E* **2020**, *102*, 052401. [CrossRef] [PubMed]
42. Xie, X.; Xu, A.M.; Angle, M.R.; Tayebi, N.; Verma, P.; Melosh, N.A. Mechanical Model of Vertical Nanowire Cell Penetration. *Nano Lett.* **2013**, *13*, 6002–6008. [CrossRef] [PubMed]
43. El-Naggar, M.Y.; Wanger, G.; Leung, K.M.; Yuzvinsky, T.D.; Southam, G.; Yang, J.; Lau, W.M.; Nealson, K.H.; Gorby, Y.A. Electrical transport along bacterial nanowires from *Shewanella oneidensis* MR-1. *Proc. Natl. Acad. Sci. USA* **2010**, *107*, 18127–18131. [CrossRef]
44. Gorby, Y.A.; Yanina, S.; McLean, J.S.; Rosso, K.M.; Moyles, D.; Dohnalkova, A.; Beveridge, T.J.; Chang, I.S.; Kim, B.H.; Kim, K.S.; et al. Electrically conductive bacterial nanowires produced by *Shewanella oneidensis* strain MR-1 and other microorganisms. *Proc. Natl. Acad. Sci. USA* **2006**, *103*, 11358–11363. [CrossRef] [PubMed]
45. Subramanian, P.; Pirbadian, S.; El-Naggar, M.Y.; Jensen, G.J. Ultrastructure of *Shewanella oneidensis* MR-1 nanowires revealed by electron cryotomography. *Proc. Natl. Acad. Sci. USA* **2018**, *115*, E3246–E3255. [CrossRef]
46. Filman, D.J.; Marino, S.F.; Ward, J.E.; Yang, L.; Mester, Z.; Bullitt, E.; Lovley, D.R.; Strauss, M. Cryo-EM reveals the structural basis of long-range electron transport in a cytochrome-based bacterial nanowire. *Commun. Biol.* **2019**, *2*, 219. [CrossRef]
47. Tripathi, A.K.; Thakur, P.; Saxena, P.; Rauniyar, S.; Gopalakrishnan, V.; Singh, R.N.; Gadhamshetty, V.; Gnimpieba, E.Z.; Jasthi, B.K.; Sani, R.K. Gene Sets and Mechanisms of Sulfate-Reducing Bacteria Biofilm Formation and Quorum Sensing with Impact on Corrosion. *Front. Microbiol.* **2021**, *12*, 754140. [CrossRef]
48. Heggendorn, F.L.; Fraga, A.G.M.; Ferreira, D.d.C.; Gonçalves, L.S.; Lione, V.d.O.F.; Lutterbach, M.T.S. Sulfate-Reducing Bacteria: Biofilm Formation and Corrosive Activity in Endodontic Files. *Int. J. Dent.* **2018**, *2018*, 8303450. [CrossRef]
49. Wen, J.; Zhao, K.; Gu, T.; Raad, I.I. A green biocide enhancer for the treatment of sulfate-reducing bacteria (SRB) biofilms on carbon steel surfaces using glutaraldehyde. *Int. Biodeterior. Biodegrad.* **2009**, *63*, 1102–1106. [CrossRef]